Reduced fatigue and leakage of ferroelectric TiN/$Hf_{0.5}Zr_{0.5}O_2$/TiN capacitors by thin alumina interlayers at the top or bottom interface

To cite this article: H Alex Hsain *et al* 2023 *Nanotechnology* **34** 125703

IOP Publishing Nanotechnology
Nanotechnology 34 (2023) 125703 (10pp) https://doi.org/10.1088/1361-6528/acad0a

Reduced fatigue and leakage of ferroelectric TiN/$Hf_{0.5}Zr_{0.5}O_2$/TiN capacitors by thin alumina interlayers at the top or bottom interface

H Alex Hsain[1,2,*], Younghwan Lee[3], Suzanne Lancaster[2], Patrick D Lomenzo[2], Bohan Xu[2], Thomas Mikolajick[2,4], Uwe Schroeder[2], Gregory N Parsons[5] and Jacob L Jones[1,*]

[1] Materials Science and Engineering Department, North Carolina State University, 911 Partners Way, Raleigh, NC, 27695 United States of America
[2] NaMLab gGmbH, Noethnitzer Strasse 64a, D-01187 Dresden, Germany
[3] Research Institute of Advanced Materials, Seoul National University, Seoul, 08826, Republic of Korea
[4] TU Dresden, Chair of Nanoelectronics, Noethnitzer Strasse 64a, D-01187 Dresden, Germany
[5] Chemical and Biomolecular Engineering Department, North Carolina State University, 911 Partners Way, Raleigh, North Carolina, NC, 27695 United States of America

E-mail: hahsain@ncsu.edu and jacobjones@ncsu.edu

Received 10 October 2022, revised 11 December 2022
Accepted for publication 19 December 2022
Published 13 January 2023

Abstract

$Hf_{0.5}Zr_{0.5}O_2$ (HZO) thin films are promising candidates for non-volatile memory and other related applications due to their demonstrated ferroelectricity at the nanoscale and compatibility with Si processing. However, one reason that HZO has not been fully scaled into industrial applications is due to its deleterious wake-up and fatigue behavior which leads to an inconsistent remanent polarization during cycling. In this study, we explore an interfacial engineering strategy in which we insert 1 nm Al_2O_3 interlayers at either the top or bottom HZO/TiN interface of sequentially deposited metal-ferroelectric-metal capacitors. By inserting an interfacial layer while limiting exposure to the ambient environment, we successfully introduce a protective passivating layer of Al_2O_3 that provides excess oxygen to mitigate vacancy formation at the interface. We report that TiN/HZO/TiN capacitors with a 1 nm Al_2O_3 at the top interface demonstrate a higher remanent polarization ($2P_r \sim 42\ \mu C\ cm^{-2}$) and endurance limit beyond 10^8 cycles at a cycling field amplitude of 3.5 MV cm^{-1}. We use time-of-flight secondary ion mass spectrometry, energy dispersive spectroscopy, and grazing incidence x-ray diffraction to elucidate the origin of enhanced endurance and leakage properties in capacitors with an inserted 1 nm Al_2O_3 layer. We demonstrate that the use of Al_2O_3 as a passivating dielectric, coupled with sequential ALD fabrication, is an effective means of interfacial engineering and enhances the performance of ferroelectric HZO devices.

Supplementary material for this article is available online

Keywords: hafnia, ferroelectric, thin film, interlayers, metal-ferroelectric-metal, Al_2O_3

(Some figures may appear in colour only in the online journal)

* Authors to whom any correspondence should be addressed.

1. Introduction

As demand for consumer electronics continues to increase in our digitalized world, there is a concurrent need for device miniaturization and enhanced functionality. Besides high-k dielectric applications, in the past ten years, hafnium oxide (HfO_2) has emerged as a viable material for ferroelectric field-effect transistors (FeFETs) [1–3], ferroelectric tunnel junctions (FTJs) [4, 5], vertical arrangements such as 3D NAND [6], and energy-related applications such as supercapacitors [7], and pyroelectric energy harvesters [8–10]. The inherently low-energy and scalable switching mechanism of ferroelectric HfO_2 makes it an attractive material for emergent computing paradigms such as edge computing [11] and neuromorphic computing [12]. For these applications, low switching voltages, wake-up free behavior, and high endurance are desirable.

The electronic functionality in HfO_2 arises from its ferroelectricity, i.e. a field-driven, reorientable spontaneous polarization in HfO_2. Ferroelectricity in HfO_2 stems from its polar orthorhombic crystal structure (space group $Pca2_1$) [13] which can be represented as a strained tetragonal phase ($P4_2/nmc$) [13]. Driving factors that have been ascribed to stabilizing the orthorhombic phase include mechanical stress from capping layers and densification [14, 15], dopants [16, 17], annealing [18–20], and substrates [21, 22]. Many have proposed that oxygen vacancies also play a critical role in stabilizing the orthorhombic phase [23–25]. First-principles calculations show that an oxygen vacancy concentration of ~2 at% in HfO_2 decreases the surface energy of the tetragonal and orthorhombic phases over the monoclinic phase by 5–10 and 5 meV f.u.$^{-1}$, respectively [26, 27], affecting the activation barrier for phase transitions [17]. Oxygen vacancies have also been identified as the main factor behind the deleterious wake-up effect [28, 29], i.e. the increase in remanent polarization with electric field cycling, as well as assisting in fatigue and eventual dielectric breakdown [29, 30].

Oxygen vacancy concentration in HfO_2 can be altered by controlling the gas environment during annealing [31–33], by altering the oxygen source [19, 34, 35] or oxygen pulse duration [25, 34], and by engineering the oxide-electrode interface [36–40]. The final listed strategy, i.e. engineering the oxide-electrode interface, has been the subject of intense investigation, given the importance of the oxide interface in determining the reliability of the device [38, 41]. Titanium nitride (TiN) electrodes are most frequently paired with ferroelectric HfO_2 as they typically result in the most favorable ferroelectric properties in HfO_2. TiN is well-known as an oxygen scavenging material where Ti favorably reacts with oxygen to form TiO_x or TiO_xN_y when in contact with an oxide. Hard x-ray photoelectron spectroscopy (HAXPES) studies have shown that when placed in contact with HfO_2, TiN acts as an oxygen sink where oxygen diffuses from the oxide and to the electrode, leaving behind positively charged oxygen vacancies [39, 41]. Pešić *et al* suggested that the fastest O vacancy defect generation occurs at the TiO_x interface between HfO_2 and TiN where electron trapping creates leakage pathways and eventually results in a breakdown of the device [29]. While the inclusion of oxygen vacancies in small concentration can be favorable for eliciting the ferroelectric phase in HfO_2, excess vacancy formation from TiN can negatively impact the endurance of HfO_2 ferroelectric devices [30, 42].

To mitigate premature degradation of ferroelectric HfO_2 devices, several authors have inserted oxide interlayers to better stabilize the HfO_2/TiN interface. Szyjka *et al* investigated the role of supplied oxygen flow either before or during the deposition of a PVD-grown HfO_2 layer and found that when oxygen is supplied to the chamber before HfO_2 growth, a self-limiting TiO_2 layer forms on TiN and chemically stabilizes the interface [39]. Most recently, Al_2O_3 has also been considered as an interlayer due to effective diffusion barrier properties [43, 44]. Filatova *et al* grew an Al_2O_3 interlayer via ALD between HfO_2 and TiN which drastically reduced the formation of TiO_x and TiO_xN_y, where scavenging of oxygen by TiN was reduced by the presence of more chemically stable Al–O bonds [40]. Theoretical studies have also reported a deeper electron trap level for Al_2O_3 compared to HfO_2, suggesting that Al_2O_3 has a lower driving force for oxygen vacancy creation compared to HfO_2 [45]. The defect mitigation properties of Al_2O_3 were leveraged by Kavrik *et al* where Al_2O_3 at the top or bottom interface showed a decrease in the interface trapped charge which they ascribed to oxygen scavenging by diffusion of trimethylaluminum (TMA, $Al(CH_3)_3$) species into HfO_2 [46]. HZO films by Alcala *et al* also showed leakage and endurance improvements with added Al_2O_3 or La_2O_3 interlayers [47].

Despite successful integration of Al_2O_3 into HfO_2-based capacitors in these aforementioned studies, a major drawback of these fabrication strategies is that TiN and HZO are deposited in separate chambers which requires vacuum breaking steps and subsequently introduces both deleterious carbon adsorption and oxidation of the electrode. In the present study, we minimize spontaneous oxidation of TiN by depositing all layers of the metal-ferroelectric-metal (MFM) capacitor in a process called sequential, no-atmosphere processing (SNAP) [31]. Given the favorable properties of Al_2O_3, e.g. a high bandgap of 6.2–6.5 eV [48], compatibility with Si, and the ability to stabilize the HfO_2/TiN via oxygen vacancy reduction, we hypothesize that insertion of a 1 nm interlayer of Al_2O_3 at either the top or bottom interface will improve the endurance and leakage characteristics of SNAP-deposited TiN/HZO/TiN devices.

Using Si as a bottom substrate, we grow Si/TiN/Al_2O_3/$Hf_{0.5}Zr_{0.5}O_2$/TiN and Si/TiN/$Hf_{0.5}Zr_{0.5}O_2$/Al_2O_3/TiN capacitors with either 1 nm Al_2O_3 at the bottom or top interface, respectively, where we maintain vacuum during all layer depositions. In this way, we achieve better control over the interfacial oxidation of HZO/TiN interfaces and mitigate the spontaneous formation of TiO_x and TiO_xN_y. We modify this process in the present work by purposefully inserting 1 nm Al_2O_3 as a passivating layer while maintaining vacuum. The bilayer capacitor thus possesses the benefits of controlled, sequential processing while also demonstrating enhanced endurance and leakage properties. We also study the effects of interlayer placement within the TiN/HZO/TiN stack and

reveal the benefits of inserting an interlayer at the top interface in order to maximize remanent polarization.

2. Methods

Capacitors consisting of Si/30 nm TiN/10 nm HZO/10 nm TiN in metal-ferroelectric-metal sequence were grown in an ALD chamber without breaking vacuum as described in Lee and Hsain *et al* [31]. HZO capacitors without an Al_2O_3 interlayer are referred to as HZO-control in the text. Other capacitors were processed identically to the HZO-control but with the addition of 1 nm Al_2O_3 at either the top (HZO/TiN) or bottom (TiN/HZO) interface. The Al_2O_3 layer was grown using Trimethylaluminum (TMA) and O_2 plasma at 300 W for 6 s at 270 °C directly preceding or following the deposition of the HZO layer. Multiple batches were produced to optimize the thickness, uniformity, and stoichiometry of HZO and Al_2O_3 films and the final recipes were combined to produce the multilayer stack. The stoichiometry of the alumina layer was confirmed via x-ray photoelectron spectroscopy (XPS) and found to be consistent with Al_2O_3 (supplemental figure S1). The capacitors into which the 1 nm Al_2O_3 is inserted at the TiN/HZO interface closest to the Si wafer are referred to as HZO-AO-Bot, whereas the capacitors into which Al_2O_3 is inserted into the HZO/TiN closest to the top electrode are referred to as HZO-AO-Top in the text. All capacitors were subjected to a rapid thermal annealing treatment at 800 °C for 30 s in N_2.

For electrical characterization, 200 μm diameter contact pads of 10 nm Ti/30 nm Pt were deposited via e-beam evaporation through a shadow mask. MFM samples were subsequently etched using standard SC1 etch of H_2O:30% H_2O_2:30% NH_4OH 50:2:1 at 50 °C for 5 min. Ferroelectric characterization was conducted using an aixACCT System TF Analyzer 3000, where each measurement was conducted on a pristine contact with no previous electrical history. For polarization-electric field (*P–E*) hysteresis characterization, measurements were taken using a bipolar triangular waveform at 1 kHz and of 1–4.5 MV cm^{-1}. The endurance measurement was conducted using a bipolar periodic square waveform with 100 kHz and an electric field amplitude of either 3.5 or 4.5 MV cm^{-1}, while a dynamic hysteresis measurement (DHM) was taken five times per decade on a log-scale (See S2 for pulse train). Dielectric permittivity was extracted from capacitance-voltage curves taken using a voltage sweep up to 3 V with a 50 mV small signal amplitude at 10 kHz. Each electrical measurement was taken at least five times on different and pristine devices to ensure repeatability. Experimental details for analytical characterization including x-ray photoelectron spectroscopy (XPS), grazing incidence x-ray diffraction (GIXRD), time-of-flight secondary ion mass spectroscopy (ToF-SIMS), and scanning transmission electron microscopy (S/TEM) are included in the Supplemental Information document.

3. Results and discussion

The arrangement of HZO-AO-Top and HZO-AO-Bot layers were verified via TEM with energy dispersive spectroscopy EDS (Talos F200X G2) and ToF-SIMS depth profiling. Figures 1(a) and (d) show schematic illustrations of the HZO-AO-Top and HZO-AO-Bot after capacitors were etched in SC1 and the top TiN electrode was dissolved, leaving behind a remaining thin TiO_xN_y interface layer. Annular bright-field scanning transmission electron microscopy (ABF-STEM) images of capacitor stacks with 1 nm Al_2O_3 layer at either the top or bottom interface are shown in figures 1(b) and (e) and indicate uniform deposition of Al_2O_3 in both configurations. EDS also confirmed the chemical presence of Al atoms at the TiN/HZO or HZO/TiN interface, with some Al signal also present in both HZO layers suggesting the diffusion of Al species either during Al_2O_3 deposition or annealing (see the overlays of Zr/Al maps). The EDS measurements are consistent with ToF-SIMS depth spectra where HZO-AO-Top and HZO-AO-Bot both demonstrated high AlO^- intensities at the respective oxide-electrode interface as well as high counts of HfO_2^-, ZrO_2, and O_2^- from 0 to 100 s sputtering time where the HZO layer is expected.

There are two key differences between HZO-AO-Top and HZO-AO-Bot ToF-SIMS spectra. First, the sputtering depth from 0 to 100 s in figure 1(f) shows an increased amount of $^{47}TiN^-$ within the HZO layer in HZO-AO-Bot, suggesting that N diffuses into the HZO layer from the top TiN layer. Second, comparing the $^{50}TiO^-$ signal at the bottom TiN/HZO interface, we see that there is more interfacial oxidation in HZO-AO-Bot (figure 1(f)) than HZO-AO-Top (figure 1(c)). To understand which electrode contributes to the Ti and N species diffusion into HZO, let us consider that the top HZO:TiN interface is typically characterized by a much thinner TiO_xN_y layer compared to the bottom interface [35, 39]. As shown by Szyjka *et al* the bottom interlayer forms during deposition of HZO on top of the TiN which results in a pronounced oxide interlayer that can prevent interfacial intermixing [39]. On the other hand, the interlayer that forms at the top HZO:TiN interface is much thinner and acts as a poor diffusion barrier against Ti and N compared to the bottom interfacial layer [35]. In the present case, the oxygen species from the Al_2O_3 layer at the bottom interface likely enhanced the growth of a more pronounced TiO_x layer at the bottom interface of HZO-AO-Bot. Thus, the observed $^{47}TiN^-$ within the HZO layer in HZO-AO-Bot likely originates from chemical species diffusing from the top TiN electrode where the thinner TiO_xN_y interface acted as a poor diffusion barrier. The converse effect is observed in HZO-AO-Top where the Al_2O_3 interlayer at the top interface acted as a good diffusion barrier and prevented diffusion of chemical species from the TiN and HZO layers to the bottom interface. The oxygen scavenging behavior observed here by ToF-SIMS is also consistent with the report from Hamouda *et al,* who showed via XPS that Hf is reduced near the top interface due to oxygen scavenging by the top TiN during the crystallization anneal [38]. Selective oxygen and nitrogen diffusion into the electrodes and HZO layer, respectively,

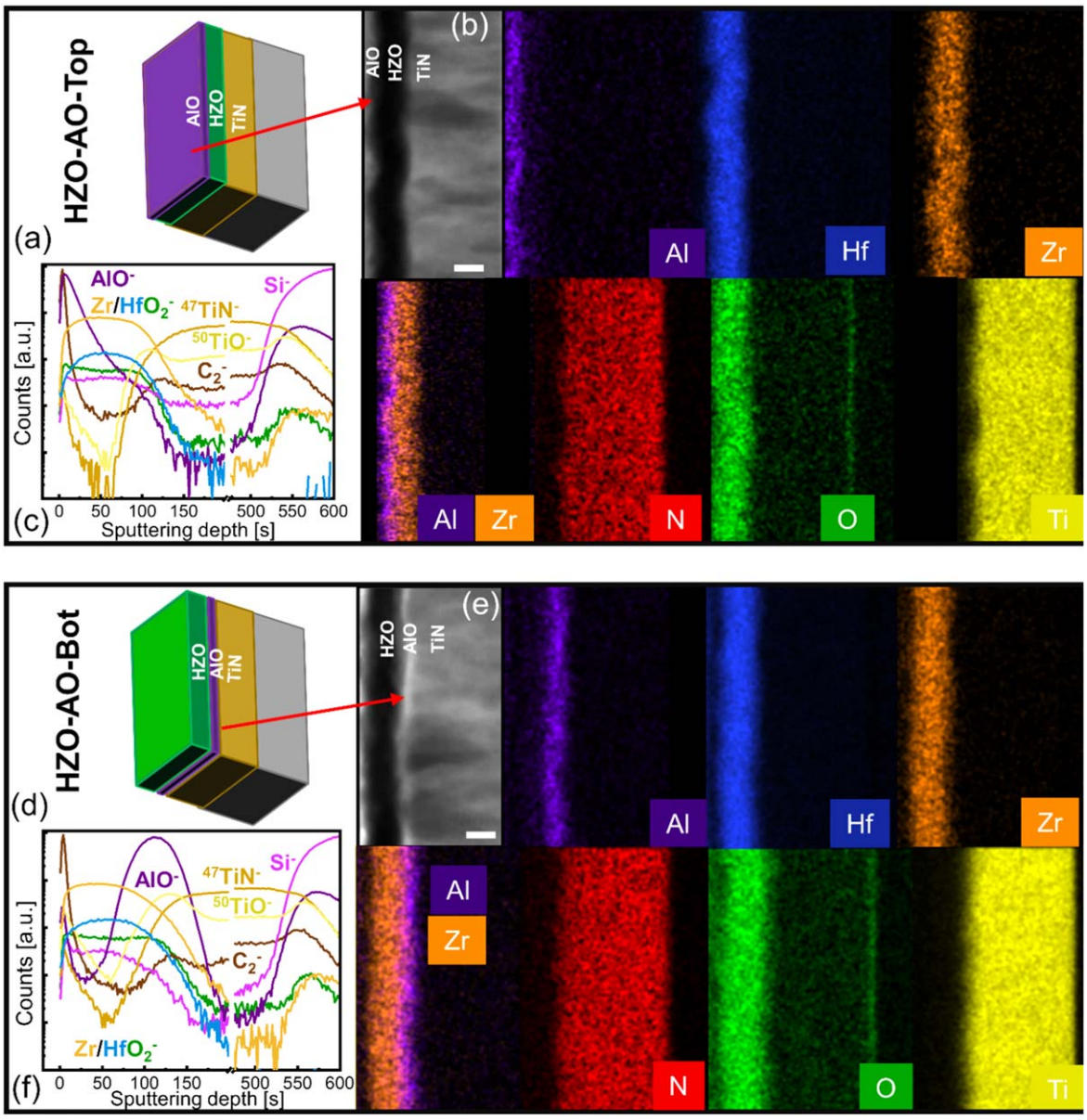

Figure 1. Schematic illustrations of (a) HZO-AO-Top and (d) HZO-AO-Bot. ToF-SIMS depth profile of (c) HZO-AO-Top and (f) HZO-AO-Bot showing Zr/HfO_2^-, AlO^- ^{47}, TiN^- ^{50}, TiO^-, C_2^-, and Si^- chemical species. Annular bright-field scanning transmission electron microscopy (ABF-STEM) images of (b) HZO-AO-Top and (e) HZO-AO-Bot including electron dispersive spectroscopy (EDS) images of Al, Hf, Zr, O, N, and Ti. The scalebar in the ABF-STEM images corresponds to 10 nm.

may lead to the formation of oxygen vacancies at the interfaces and unintentional N-doping, both of which have been shown to influence the structural and electrical properties of HZO capacitors [37, 49].

The phases and preferred orientation of multilayer capacitor stacks of HZO-control, HZO-AO-Bot, and HZO-AO-Top was investigated via GIXRD after annealing at 800 °C for 30 s in N_2 shown in figure 2. Intensities are normalized to the integrated intensity of the 200 reflection of TiN to better perceive the intensity differences among films, while the diffraction geometry was kept constant across all measurements. All samples demonstrated a GIXRD pattern consistent with mixed phase of orthorhombic and/or tetragonal based on the presence of the overlapping orthorhombic 111 reflection (referred herein as o111) and tetragonal 011 reflection (referred herein as t011). Because the o111 and t011 are so closely overlapping, it is difficult to discriminate between these two phases; thus, the peak at $2\theta \sim 30°$ is typically reported as o111/t011 in the literature, which we shorthand as o111 in this text, as we believe the films to be predominately composed of the orthorhombic phase. A peak at ~35° is present in both films and corresponds to a combination of the tetragonal 110 and/or orthorhombic 200, 020, and 002 reflections, herein collectively referred to as o{002}. No non-ferroelectric monoclinic phase was observed in any multilayer sample. A sharp peak near 52° observed in HZO-AO-Top and HZO-AO-Bot is ascribed to the 311 reflection from the Si wafer.

While diffraction patterns from the three sample were very similar, slight differences in the integrated area of o111

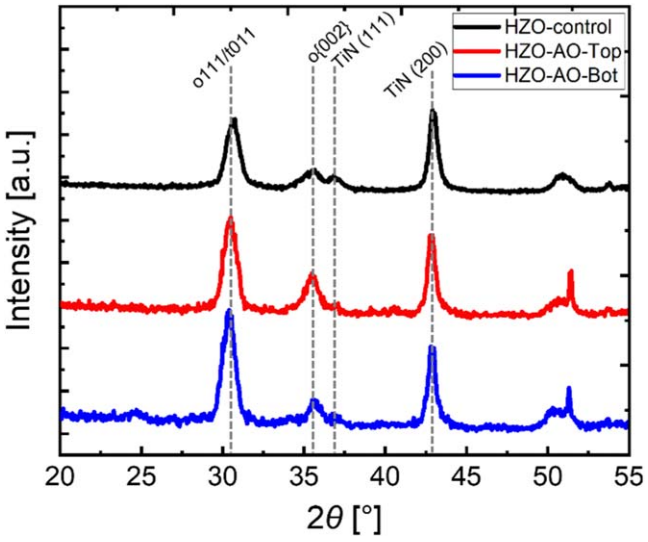

Figure 2. Grazing incidence XRD (GIXRD) patterns of HZO-control (top black), HZO-AO-Top (middle red) and HZO-AO-Bot (bottom blue) annealed at 800 °C. Intensities are normalized to the 002 integrated peak of TiN; The reference XRD patterns of HZO phases are orthorhombic (PDF #: 04-005-5597) and tetragonal (PDF #: 04-011-8820).

and o{002} peaks revealed possible differences in phase composition and/or crystallographic texture. Each peak was fit to a Pearson-VII model profile shape function using LIPRAS software (not shown) [50]. The integrated intensity ratio of the o111:o{002} peak in HZO-AO-Bot was found to be twice the value of HZO-AO-Top, whereas the o111:o{002} peak ratio of HZO-AO-Top was found to be approximately the same as HZO-control. The higher o111:o{002} peak ratio in HZO-AO-Bot is consistent with 111 fiber texture where the Al_2O_3 interlayer may have encouraged the growth of more energetically favorable HZO {111} planes parallel to the film surface because they have a lower surface energy compared to the {001} planes [51]. Though the degree of texture cannot be discerned via GIXRD alone, the present data suggests that the insertion and placement of an interlayer can influence phase composition and/or encourage the development of different textures in HZO films which is consistent with our earlier findings [35].

Figure 3 displays *P–E* loops as a function of electric field cycling for HZO-control, HZO-AO-Top, and HZO-AO-Bot. In figure 3(a) the remanent polarization $2P_r$ value shows an increase from 50 μC cm^{-2} to 54 μC cm^{-2} after 10^4 cycles. Given the nonlinear increase in current density at high field amplitudes, the increase in $2P_r$ value is likely due to de-pinning of domain walls and the concurrent increase in charge injection. The $2P_r$ of HZO-AO-Top in figure 3(b) remains relatively stable at ~42 μC cm^{-2} during cycling. In figure 3(c) the $2P_r$ for HZO-AO-Bot increases from 33 μC cm^{-2} to 42 after 10^4 cycles. Note that in the pristine state HZO-AO-Bot demonstrates two prominent switching peaks but after sufficient wake-up cycling, i.e. 10^2 cycles, the switching peaks begin to merge. The presence of this double peak feature and consequently, wake-up, suggests that HZO-AO-Bot films possess a higher tetragonal phase fraction than HZO-control or HZO-AO-Top. In HZO-AO-Top, on the other hand, the $2P_r$ and *J–E* loop remain stable, suggesting that placement of a top interlayer in HZO-AO-Top more readily mitigated the wake-up effect.

The $2E_c = |E_{c-}| + E_{c+}$ after 10^4 cycles is determined for all three cases where HZO-control has a $2E_c$ value of 3.3 MV cm^{-1} compared to 3.8 MV cm^{-1} for HZO-AO-Bot. Accordingly, the field drop on the ferroelectric layer is up to 38% lower for the samples with the bottom Al_2O_3 interlayer; it follows that a lower amount of charge injection and charge movement is expected during switching. On the other hand, HZO-AO-Top showed a broad switching peak and a $2E_c$ of 3.2 MV cm^{-1}, which is nearly equivalent to the $2E_c$ of HZO-control. It is expected that in HZO-control the TiN readily reacts with the oxide-rich HZO layer to form a TiO_xN_y layer. One explanation for the similar $2E_c$ values of HZO-control and HZO-AO-Top is that, in the latter case, the top Al_2O_3 layer may reduce oxygen diffusion from HZO into the top TiN; therefore, the additional Al_2O_3 thickness is compensated by less TiO_x formation at the top interface [38]. HZO-AO-Bot, on the other hand, possesses both the native TiO_xN_y oxidation at the top interface as well as the additional Al_2O_3 oxide at the bottom interface, which leads to the observed higher $2E_c$.

Figure 4 displays ε_r-E behaviors as a function of cycle number (for films cycled with an electric field amplitude of 3.5 MV cm^{-1}) for HZO-control, HZO-AO-Top, and HZO-AO-Bot. In all three cases the permittivity of the ferroelectric layer at the most extreme DC bias field of 3.0 MV cm^{-1}, i.e. the field at which domain switching contributions are minimized, is in the range of 26–27. The lower ε_r exhibited in capacitors with Al_2O_3 interlayers is due to the lower dielectric constant value of $Al_2O_3 \sim 9$ where the additional layer acts as a dielectric in series with HZO and diminishes the overall capacitance [46, 52]. Figure 4(a) shows permittivity as a function of DC bias offset for the HZO-control capacitor after different numbers of cycles. The permittivity at a DC bias field near the coercive field ($\varepsilon_{r,c}$) remains relatively constant from the pristine state to the 10^2 cycled state, which is consistent with prior observations of no wake-up effect in SNAP-processed capacitors [31]. After 10^4 cycles, the $\varepsilon_{r,c}$ value decreases, suggesting a reduction in realizable switched polarization due to pinned or locked domains [29]. After 10^5 cycles, HZO-control experiences dielectric breakdown. Similarly, figure 4(b) shows that the $\varepsilon_{r,c}$ of HZO-AO-Top decreases upon cycling. It is also interesting to note the asymmetrical pinching of the ε_r-E loop at −2.2 V, which likely originates from the non-symmetrical oxide-electrode interfaces. Figure 4(d) of HZO-AO-Bot shows a small decrease in $\varepsilon_{r,c}$ with increased cycling and an asymmetrical pinching of the ε_r-E loop in the positive bias region near 2 V. The upward tail bending in the permittivity loops of capacitors with an Al_2O_3 layers suggest more pronounced leakage contribution compared to HZO-control. The decrease in permittivity as a function of field cycling shown in figures 4(a)–(c) evidences the progression of fatigue. Phenomenologically, in PZT-based ferroelectric thin films, several mechanisms have described fatigue behavior, including

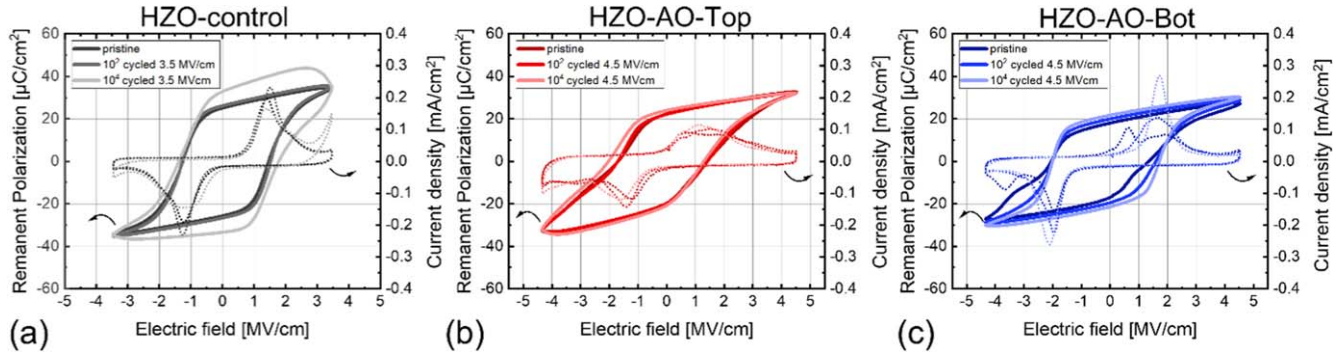

Figure 3. Polarization versus electric-field (*P*–*E*) loops with overlaying current density versus electric-field (*J*–*E*) loops as a function of field cycling acquired from (a) HZO-AO-control, (c) HZO-AO-Top, and (e) HZO-AO-Bot.

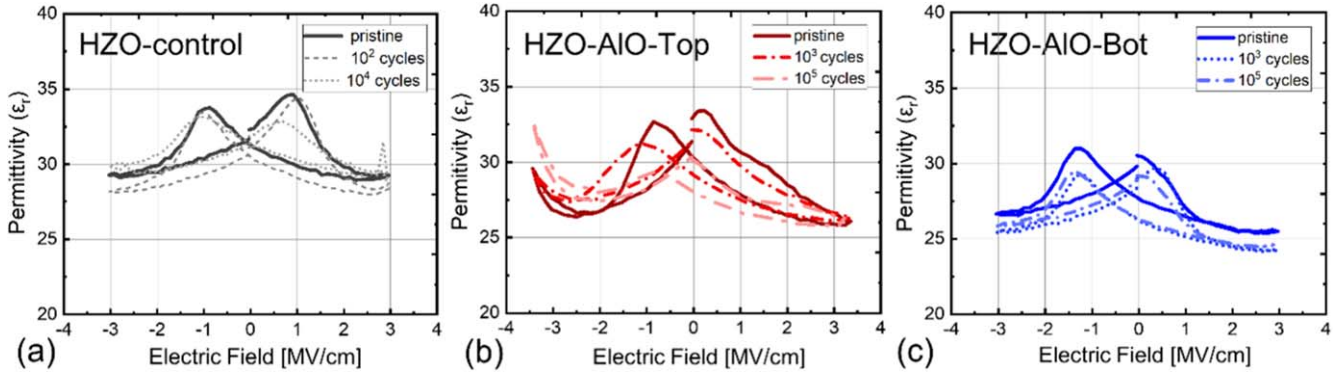

Figure 4. Permittivity versus DC bias electric-field amplitude (ε_r-E) as a function of cycle number with an electric field amplitude of 3.5 MV cm^{-1} acquired from (b) HZO-AO-control, (d) HZO-AO-Top, and (f) HZO-AO-Bot.

domain wall pinning [53], seed inhibition mechanism [53], local imprint [54], and local phase deposition mechanism [55], while microscopic models pointed toward mechanisms of oxygen vacancy redistribution [29] and charge injection [54]. Permittivity as a function of applied DC bias field is known to capture a combination of intrinsic (lattice, ionic) and extrinsic (domain wall, defects) contributions to dielectric response and can be at least partly de-convoluted by observing the response at the saturating and coercive field, respectively.

First we consider the intrinsic, or lattice, contribution to permittivity. The ε_r at saturating fields near ± 3 V remains approximately constant for HZO-control and HZO-AO-Top as a function of field cycling. In the seed-inhibition model, the ε_r is expected to only change near the coercive field where domain walls are still able to contribute via bending [53]. The nearly constant ε_r at saturating electric fields in HZO-AO-Top and HZO-control permittivity loops suggest that the seed inhibition mechanism, where domain walls stop participating in the overall switching process and results in a loss of polarization, may also be at play in capacitors with a more pristine bottom TiN/HZO interfaces.

Now we consider the extrinsic contribution to permittivity measured at lower electric fields. In capacitors both with and without an Al_2O_3 interlayer, the permittivity at E_c (enhanced by the extrinsic contribution) decreases as a function of cycling. One possible mechanism for the monotonic decrease of the permittivity at E_c with increased cycling may be domain wall pinning by which domains become immobilized due to charged defects accumulated at oxide-electrode interfaces. Electrostatic coupling causes mobile charge carriers to combine with bound charges to create charge-neutral defect complexes, which then prevent polarization switching [56]. Additionally, given the increase in leakage current density as a function of cycling, domains could become pinned due to increased electric field-induced trap density generation at higher cycling numbers [29]. Electrons trapped at interfacial regions close to the electrodes alter the field distribution within the stack and cause the rise of internal fields, which suppresses ferroelectric switching. The increase in defects and vacancies creates leakage pathways and finally results in the dielectric breakdown of the device.

Finally we consider the extrinsic contribution for HZO-AO-Bot. The decreasing ε_r near the coercive field with cycling suggests that HZO undergoes an electric-field induced phase transformation. Recent studies have shown that a reversible structural transformation from the polar to antipolar phase may account for the observed wake-up and fatigue in HZO capacitors [57]. In the present case, we observe a decrease in the permittivity with cycling measured at DC bias fields near the coercive field of HZO-AO-Bot, which suggests a partial phase transformation from the high permittivity tetragonal phase ($\varepsilon_r \sim 36$–40) to the lower permittivity orthorhombic phase ($\varepsilon_r \sim 30$) [58]. The decrease in permittivity is consistent with the observed wake-up effect in HZO-AO-Bot

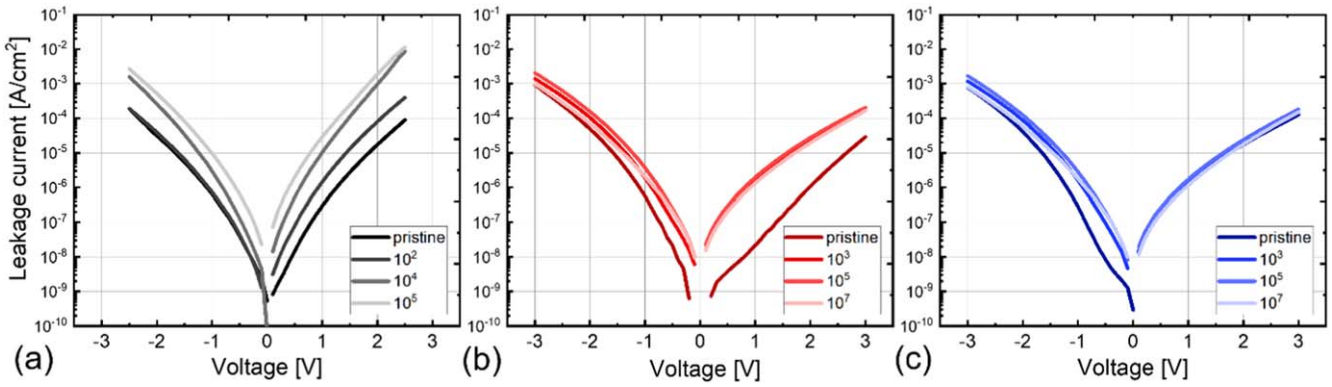

Figure 5. Leakage current density in the pristine state and after 10^3, 10^5, and 10^7 electric field cycles with an electric field amplitude of 3.5 MV cm^{-1} for capacitors (a) HZO-control (grey), (b) HZO-AO-Top (red) (c) HZO-AO-Bot (blue).

in figure 3(c). Finally we consider that the overall decrease in permittivity (both in the extrinsic and intrinsic regions) is only observed for HZO-AO-Bot which is also the only sample with wake-up. This behavior is consistent with prior reports which ascribe the phase transformation from the antipolar tetragonal phase to the polar orthorhombic as the origin of wake-up [29, 59]. In summary, the data presented here suggests that the incorporation of a top interfacial layer, compared to a bottom layer, better mitigates the wake-up effect in HZO-based capacitors.

Figure 5 shows the leakage current density of HZO-control, HZO-AO-Top, and HZO-AO-Bot taken after cycling at 3.5 MV cm^{-1} for multiple decades. Note the asymmetry present in the leakage current density curves in pristine capacitors; HZO-AO-Top shows lower leakage current density in the positive bias region, whereas HZO-AO-Bot shows a lower leakage current density in the negative bias region. The asymmetries present in figures 5(b) and (c) likely stem from the asymmetrical interfaces within the capacitor as was seen in permittivity curves in figure 4. The overall leakage current density decreases when Al_2O_3 was inserted in either the top or bottom interface and remained relatively more stable with prolonged cycling in contrast to HZO-control. At 2 V, to reach a leakage current density of 1×10^{-5} A cm^{-2}, HZO-AO-Top and HZO-AO-Bot required 10^7 cycles. On the other hand, only 10^5 cycles were required for HZO-control to result in a higher leakage current density of 1×10^{-3} A cm^{-2}. Based on these observations, we find that the placement of 1 nm Al_2O_3 at either top or bottom oxide-electrode interface is to be a viable method for decreasing leakage current density in HZO-based capacitors both in the pristine state and after electric-field cycling.

Figure 6 shows the endurance characteristics of HZO-control, HZO-AO-Top, and HZO-AO-Bot cycled at two field amplitudes and measured up to 10^8 cycles. HZO-control endured 2×104 cycles at 3.5 MV cm^{-1} before experiencing dielectric breakdown. Compared to HZO-control, both HZO-AO-Bot and HZO-AO-Top show a higher endurance limit by up to two decades at a cycling field of 4.5 MV cm^{-1}. The endurance of both HZO-AO-Bot and HZO-AO-Top is further extended by several decades at a cycling field of 3.5 MV cm^{-1} where a relatively high $2P_r$ of 40 μC cm^{-2} was

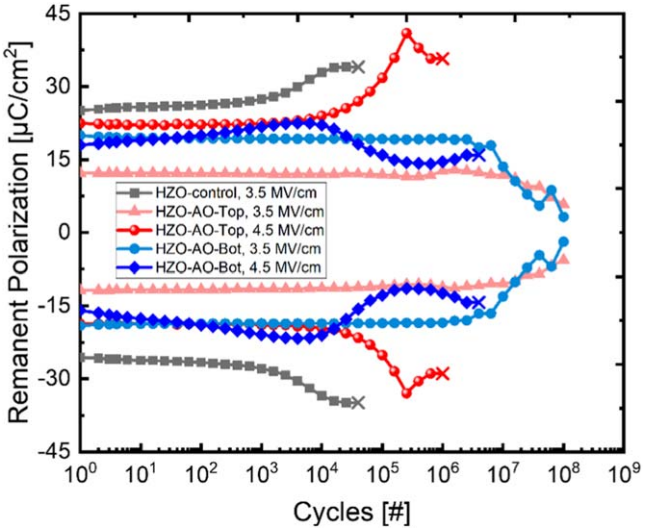

Figure 6. Endurance measurements at a cycling field of 3.5 MV cm^{-1} and 4.5 MV cm^{-1} for TiN/HZO/TiN capacitors with no Al_2O_3 interface (grey), 1 nm Al_2O_3 layer at the top interface, HZO-AO-Top (red), and 1 nm Al_2O_3 layer at the bottom interface, HZO-AO-Bot (blue). '*X*' symbol denotes the cycle number that the sample experienced dielectric breakdown during the measurement.

maintained for HZO-AO-Bot. When cycled at lower voltages, i.e. 3.5 MV cm^{-1}, the $2P_r$ significantly decreases for HZO-AO-Top, as shown in figure S3, likely due to incomplete switching.

Factors that may explain the improved endurance with the inclusion of Al_2O_3 into HZO capacitors include (1) the reduction of interface trapped charge and (2) a decrease in oxygen-related defects. Several studies have suggested that the reduction of leakage current density in HfO_2-based devices with the inclusion of an alumina buffer layer stems from how the Al_2O_3 layer interacts with oxygen defects in HZO [52, 60, 61]. It is well-known that TiO_x forms at the TiN/HZO interface where oxygen diffuses from the HZO layer to the oxide-electrode and reacts with metallic Ti [29, 52]. The formation of TiO_x occurs when gettering TiN acts as an oxygen sink and pulls oxygen from the HZO layer leaving behind oxygen vacancies. One way to mitigate the flux of oxygen from HZO is to insert an additional oxide layer

to stabilize the HZO/TiN interface. Interfacial engineering strategies such as the use of O_2 plasma or vacuum breaking during growth of TiN/HZO/TiN capacitors, e.g. as by Hsain *et al,* [35], have shown to be effective in promoting increased device endurance. The observed higher endurance could also be driven by the presence of a non-orthorhombic phase adjacent to the HZO film. Song *et al* elucidated how a non-orthorhombic phase in HZO films could enhance endurance by decreasing domain wall pinning [62]. Considering the Al_2O_3 layer specifically, Kavrik *et al* proposed that the mechanism by which the reduction of interface trapped charge (D_{it}) occurred in HfO_2/Al_2O_3 interfaces was via oxygen scavenging, where diffusion of TMA precursor species into HfO_2 reduced oxygen defects at the oxide-electrode interface [46]. While previous reports ascribe the diminished D_{it} in HZO/Al_2O_3 structures to the beneficial diffusion barrier properties of Al_2O_3, Kavrik *et al* correlated the reduction in D_{it} to oxygen scavenging electrodes reacting with Al_2O_3 within the capacitor stack. Similarly, in the present study, the improved endurance in multilayer capacitors with Al_2O_3 interlayers is likely the result of Al_2O_3 reducing the oxygen vacancy defects originating from gettering TiN. Theoretical studies also point toward the lower propensity for oxygen vacancy formation in Al_2O_3 as compared to HfO_2. Liu *et al* used the screened exchange hybrid functional model to calculate the trapped electron level in Al_2O_3 to be 1.8 eV, whereas in HfO_2 the trapped electron level was found to be 0.4 eV. Given the deeper transport depth of Al_2O_3 for the formation of O vacancy determined by Liu *et al* there exists a lower driving force for vacancy creation in Al_2O_3 compared to HfO_2, which gives rise to the beneficial properties of using Al_2O_3 as a stabilizing interlayer at oxide-electrode interfaces.

Now we discuss the differences in $2P_r$ and wake-up behavior between HZO-AO-Top and HZO-AO-Bot. HZO-AO-Bot showed a more pronounced wake-up effect at 4.5 MV cm^{-1} and a higher $2P_r$ value at the lower cycling field of 3.5 MV cm^{-1}. The more pronounced wake-up in HZO-AO-Bot likely stems from a higher tetragonal phase composition as was suggested by the measured higher permittivity in the pristine state. It is well-known that the underlying templating layer can promote or inhibit the development of small HZO crystal nuclei [35, 63, 64]. Park *et al* found that HZO nanolaminates grown on ZrO_2-starting layers resulted in a higher monoclinic phase fraction due to the tensile strain exerted by the first-crystallized ZrO_2 underlayer, which possesses a larger lattice parameter than HfO_2 [65]. The deposition of HfO_2 on top of an Al_2O_3 interlayer may elicit the development of small nuclei during the ALD process which would result in the premature crystallization of the HZO film in the ALD chamber. The small initial nuclei likely crystallize in the tetragonal phase and promote the development of a higher tetragonal phase portion during annealing. Given that wake-up has been ascribed to an electric-field induced phase transformation from the tetragonal to the orthorhombic phase, it seems plausible that the origin of heightened wake-up in HZO-AO-Bot stems from the differing seed layer morphology which favored the development of a higher concentration of the tetragonal phase.

We also revisit the observed differences in $2P_r$ between HZO-AO-Top and HZO-AO-Bot at a cycling field of 3.5 MV cm^{-1}. Note that HZO-AO-Bot does not experience wake-up at this lower cycling field, suggesting that the activation barrier for the tetragonal to orthorhombic electric-field induced phase transformation has not been reached; thus, sub-cycling i.e. cycling below the saturating electric field, avoids the deleterious wake-up phenomenon in HZO capacitors with Al_2O_3 interlayers. To explain the differences in $2P_r$ at 3.5 MV cm^{-1} between HZO-AO-Top and HZO-AO-Bot, we consider the effectiveness of Al_2O_3 as a diffusion barrier and its consequences on unintentional doping of HZO. As was shown in the ToF-SIMS analysis, the HZO-AO-Bot sample possessed higher counts of $^{47}TiN^-$ and $^{50}TiO^-$ within the HZO layer compared to HZO-AO-Top suggesting that placement of the Al_2O_3 layer can directly influence the diffusion of N and O chemical species. Xu *et al* found as little as 0.34 at% of N doping was able to increase the $2P_r$ in HZO from 40 to 50 μC cm^{-2} [49]. A similar mechanism may be found in HZO-AO-Bot in which chemical species from the top TiN layer diffuse into HZO during annealing treatment. In HZO-AO-Top, the Al_2O_3 layer instead blocks the diffusion of N or O species from the top TiN electrode into the HZO layer and results in a more pristine TiN/HZO interface with a less pronounced TiO_xN_y. Hamouda *et al* showed that in TiN/HZO/TiN capacitors, the top electrode could scavenge O atoms from the HZO layer, oxidizing the electrode material and forming an oxygen-depleted layer in the ferroelectric [38]. The addition of Al_2O_3 to the top interface not only limits N diffusion but could also mitigate oxygen vacancy formation at the top interface, which could also lower the $2P_r$. At a higher cycling field of 4.5 MV cm^{-1} when capacitors are no longer being sub-cycled, the differences in chemical profiles and doping become insignificant such that the $2P_r$ becomes comparable between HZO-AO-Top and HZO-AO-Bot.

4. Conclusion

We report the growth of TiN/HZO/TiN multilayer capacitors with 1 nm Al_2O_3 at either the top or bottom HZO-TiN interfaces grown sequentially in the ALD reactor. TiN/HZO/TiN capacitors with 1 nm at the bottom TiN/HZO interface demonstrated superior endurance properties, lasting up to 10^8 cycles without experiencing a dielectric breakdown. HZO capacitors with a 1 nm Al_2O_3 layer at either the top or bottom interface achieved a $2P_r$ of ~42 μC cm^{-2}. ToF-SIMS and EDS suggested N diffusion into the HZO layer with the 1 nm Al_2O_3 layer placed at the bottom interface, which may have favorably affected the ferroelectricity at low cycling fields. In addition, deposition of a top Al_2O_3 could have suppressed the premature crystallization of HZO into the non-ferroelectric tetragonal phase and instead aided the development of the orthorhombic phase upon rapid thermal annealing. Both capacitors with a top or bottom 1 nm Al_2O_3 layer showed robust leakage current density properties of $\sim 10^{-5}$ A cm^{-2} after 10^7 cycles at 3.5 MV cm^{-1}. The favorable properties of Al_2O_3 allow it to provide oxygen to adjacent layers and act as

a diffusion barrier. Al_2O_3 interlayers stabilize the HZO/TiN interface and suppresses oxygen vacancy formation, which leads to the observed improved endurance and leakage properties in ferroelectric HZO capacitors. Our work illustrates that, in combination with a sequential deposition of the capacitor stack without breaking vacuum, inserting Al_2O_3 to stabilize the interfaces is a viable interfacial engineering strategy for HZO devices.

Acknowledgments

This contribution is based upon the work supported by the National Science Foundation (NSF), as part of the Center for Dielectrics and Piezoelectrics under Grant Nos. IIP-1841453 and IIP-1841466. HAH was supported by the National Science Foundation Graduate Research Fellowship Program (No. DGE-1746939), an INTERN supplemental grant, and the IIE-GIRE Program funded by the National Science Foundation (No. 1829436). This work was performed at the Analytical Instrumentation Facility (AIF) at North Carolina State University and at the NC State Nanofabrication Facility (NNF), both of which are supported by the State of North Carolina and the National Science Foundation (Award No. ECCS-2025064). AIF and NNF are members of the North Carolina Research Triangle Nanotechnology Network (RTNN), a site in the National Nanotechnology Coordinated Infrastructure (NNCI). PD L, RA, and BX acknowledge the support by the Deutsche Forschungs Gemeinschaft DFG within the following projects (Zeppelin (433647091) and HOMER (430054035)). SL acknowledges funding through the European Union in the BeFerroSynaptic project (GA: 871737), and through the DFG for the projects SOgraphMEM (MI 1247/18-1) and ReLoFemRis (SL 305/2-1). US and TM were financially supported out of the Saxonian State budget approved by the delegates of the Saxon State Parliament.

Data availability statement

All data that support the findings of this study are included within the article (and any supplementary files).

ORCID iDs

H Alex Hsain https://orcid.org/0000-0002-6745-829X

References

[1] Mulaosmanovic H, Breyer E T, Dünkel S, Beyer S, Mikolajick T and Slesazeck S 2021 *Nanotechnology* **32** 502002
[2] Martin D *et al* 2013 *Solid-State Electronics* **88** 65
[3] Muller J *et al* 2013 *2013 IEEE Int. Electron Devices Meeting* (IEEE) *(Washington, DC, USA)* pp 8.1–8.4
[4] Ryu H, Wu H, Rao F and Zhu W 2019 *Sci. Rep.* **9** 20383
[5] Goh Y and Jeon S 2018 *Nanotechnology* **29** 335201
[6] Florent K *et al* 2018 *2018 IEEE Int. Electron Devices Meeting (IEDM)* (IEEE) *(San Francisco, CA)* pp 5.1–5.4
[7] Lomenzo P D, Chung C-C, Zhou C, Jones J L and Nishida T 2017 *Appl. Phys. Lett.* **110** 232904
[8] Hanrahan B, Mart C, Kämpfe T, Czernohorsky M, Weinreich W and Smith A 2019 *Energy Technol.* **7** 1900515
[9] Pandya S, Velarde G, Zhang L and Martin L W 2018 *Phys. Rev. Mater.* **2** 124405
[10] Mart C, Kühnel K, Kämpfe T, Zybell S and Weinreich W 2019 *Appl. Phys. Lett.* **114** 102903
[11] Covi E *et al* 2021 *2021 IEEE Int. Symp. on Circuits and Systems (ISCAS)* (IEEE) *(Daegu, Korea)* pp 1–5
[12] Oh S, Hwang H and Yoo I K 2019 *APL Mater.* **7** 091109
[13] Sang X, Grimley E D, Schenk T, Schroeder U and LeBeau J M 2015 *Appl. Phys. Lett.* **106** 162905
[14] Lin Y-C, McGuire F and Franklin A D 2018 *J. Vac. Sci. Technol* B **36** 011204
[15] Shimizu T, Mimura T, Kiguchi T, Shiraishi T, Konno T, Katsuya Y, Sakata O and Funakubo H 2018 *Appl. Phys. Lett.* **113** 212901
[16] Batra R, Huan T D, Rossetti G A and Ramprasad R 2017 *Chem. Mater.* **29** 9102
[17] Materano M, Lomenzo P D, Kersch A, Park M H, Mikolajick T and Schroeder U 2021 *Inorg. Chem. Front.* **8** 2650
[18] Bouaziz J, Rojo Romeo P, Baboux N, Negrea R, Pintilie L and Vilquin B 2019 *APL Mater.* **7** 081109
[19] Hyuk Park M, Joon Kim H, Jin Kim Y, Lee W, Kyeom Kim H and Seong Hwang C 2013 *Appl. Phys. Lett.* **102** 112914
[20] Chernikova A, Kozodaev M, Markeev A, Matveev Y, Negrov D and Orlov O 2015 *Microelectron. Eng.* **147** 15
[21] Li T *et al* 2018 *J. Mater. Chem.* C **6** 9224
[22] Estandía S, Dix N, Gazquez J, Fina I, Lyu J, Chisholm M F, Fontcuberta J and Sánchez F 2019 *ACS Appl. Electron. Mater.* **1** 1449
[23] Mittmann T, Materano M, Chang S-C, Karpov I, Mikolajick T and Schroeder U 2020 *2020 IEEE Int. Electron Devices Meeting (IEDM)* (IEEE) *(San Francisco, CA, USA)* pp 4.1–4.4
[24] Materano M, Mittmann T, Lomenzo P D, Zhou C, Jones J L, Falkowski M, Kersch A, Mikolajick T and Schroeder U 2020 *ACS Appl. Electron. Mater.* **2** 3618
[25] Schroeder U, Materano M, Mittmann T, Lomenzo P D, Mikolajick T and Toriumi A 2019 *Jpn. J. Appl. Phys.* **58** SL0801
[26] Hoffmann M, Schenk T, Kulemanov I, Adelmann C, Popovici M, Schroeder U and Mikolajick T 2015 *Ferroelectrics* **480** 16
[27] Lee C-K, Cho E, Lee H-S, Hwang C S and Han S 2008 *Phys. Rev.* B **78** 012102
[28] Starschich S, Menzel S and Böttger U 2016 *Appl. Phys. Lett.* **108** 032903
[29] Pešić M *et al* 2016 *Adv. Funct. Mater.* **26** 4601
[30] Molina-Reyes J, Hoshii T, Ohmi S-I, Funakubo H, Hori A, Fujiwara I, Wakabayashi H, Tsutsui K and Kakushima K 2020 *Jpn. J. Appl. Phys.* **59** SGGB06
[31] Lee Y, Alex Hsain H, Fields S S, Jaszewski S T, Horgan M D, Edgington P G, Ihlefeld J F, Parsons G N and Jones J L 2021 *Appl. Phys. Lett.* **118** 012903
[32] Chernikova A G, Kuzmichev D S, Negrov D V, Kozodaev M G, Polyakov S N and Markeev A M 2016 *Appl. Phys. Lett.* **108** 242905
[33] Mohit, Murakami T, Haga K and Tokumitsu E 2020 *Jpn. J. Appl. Phys.* **59** SPPB03
[34] Alcala R, Richter C, Materano M, Lomenzo P D, Zhou C, Jones J L, Mikolajick T and Schroeder U 2021 *J. Phys. D: Appl. Phys.* **54** 035102

[35] Hsain H A, Lee Y, Lancaster S, Materano M, Alcala R, Xu B, Mikolajick T, Schroeder U, Parsons G N and Jones J L 2022 *ACS Appl. Mater. Interfaces* acsami.2c11073
[36] Fields S S *et al* 2021 *Adv. Mater. Interfaces* **8** 2100018
[37] Filatova E O, Sakhonenkov S S, Konashuk A S, Kasatikov S A and Afanas'ev V V 2019 *J. Phys. Chem.* C **123** 22335
[38] Hamouda W, Pancotti A, Lubin C, Tortech L, Richter C, Mikolajick T, Schroeder U and Barrett N 2020 *J. Appl. Phys.* **127** 064105
[39] Szyjka T, Baumgarten L, Mittmann T, Matveyev Y, Schlueter C, Mikolajick T, Schroeder U and Müller M 2020 *ACS Appl. Electron. Mater.* **2** 3152
[40] Filatova E O, Sakhonenkov S S, Konashuk A S and Afanas'ev V V 2018 *Phys. Chem. Chem. Phys.* **20** 27975
[41] Baumgarten L, Szyjka T, Mittmann T, Materano M, Matveyev Y, Schlueter C, Mikolajick T, Schroeder U and Müller M 2021 *Appl. Phys. Lett.* **118** 032903
[42] Kozodaev M G, Chernikova A G, Korostylev E V, Park M H, Khakimov R R, Hwang C S and Markeev A M 2019 *J. Appl. Phys.* **125** 034101
[43] Cooper R, Upadhyaya H P, Minton T K, Berman M R, Du X and George S M 2008 *Thin Solid Films* **516** 4036
[44] Nehm F *et al* 2016 *Org. Electron.* **38** 84
[45] Liu D, Clark S J and Robertson J 2010 *Appl. Phys. Lett.* **96** 032905
[46] Kavrik M S, Ercius P, Cheung J, Tang K, Wang Q, Fruhberger B, Kim M, Taur Y, McIntyre P C and Kummel A C 2019 *ACS Appl. Mater. Interfaces* **11** 15111
[47] Alcala R, Mehmood P, Vishnumurthy P, Mittmann T, Mikolajick T and Schroeder U 2022 *2022 IEEE Int. Memory Workshop (IMW)* pp 1–4
[48] Afanas'ev V V and Stesmans A 2007 *J. Appl. Phys.* **102** 081301
[49] Xu L, Nishimura T, Shibayama S, Yajima T, Migita S and Toriumi A 2016 *Appl. Phys. Express* **9** 091501
[50] Esteves G, Ramos K, Fancher C and Jones J 2017 *LIPRAS: Line-Profile Analysis Software* (https://doi.org/10.13140/RG.2.2.29970.25282/3)
[51] Christensen A and Carter E A 1998 *Phys. Rev.* B **58** 8050
[52] Chen H, Tang L, Liu L, Chen Y, Luo H, Yuan X and Zhang D 2021 *Appl. Surf. Sci.* **542** 148737
[53] Colla E L, Taylor D V, Tagantsev A K and Setter N 1998 *Appl. Phys. Lett.* **72** 2478
[54] Grossmann M, Lohse O, Bolten D, Boettger U, Waser R, Hartner W, Kastner M and Schindler G 2000 *Appl. Phys. Lett.* **76** 363
[55] Lou X J, Zhang M, Redfern S A T and Scott J F 2006 *Phys. Rev. Lett.* **97** 177601
[56] Huang F *et al* 2017 *Phys. Chem. Chem. Phys.* **19** 3486
[57] Cheng Y *et al* 2022 *Nat. Commun.* **13** 645
[58] Mittmann T *et al* 2021 *Phys. Status Solidi RRL* **15** 2100012
[59] Fields S S, Smith S W, Jaszewski S T, Mimura T, Dickie D A, Esteves G, David Henry M, Wolfley S L, Davids P S and Ihlefeld J F 2021 *J. Appl. Phys.* **130** 134101
[60] Im S, Kang S-Y, Kim Y, Kim J H, Im J-P, Yoon S-M, Moon S E and Woo J 2020 *Micromachines* **11** 910
[61] Das D, Gaddam V and Jeon S 2021 *JSTS* **21** 62
[62] Song T, Estandía S, Tan H, Dix N, Gàzquez J, Fina I and Sánchez F 2022 *Adv Elect Mater.* **8** 2100420
[63] Onaya T, Nabatame T, Sawamoto N, Ohi A, Ikeda N, Nagata T and Ogura A 2019 *APL Mater.* **7** 061107
[64] Gaddam V, Das D and Jeon S 2020 *IEEE Trans. Electron Devices* **67** 745
[65] Park M H *et al* 2019 *Appl. Phys. Rev.* **6** 041403